Chapter VIII

DIVERTOR AND DIVERTOR PLATES

M.A. ABDOU	–	USA
T. HIRAOKA	–	Japan
D. LEGER	–	Euratom
N. MIKI	–	Japan
G.D. MORGAN	–	USA
Y. SAWADA	–	Japan
P. SCHILLER	–	Euratom
D.V. SEREBRENNIKOV	–	USSR
G.E. SHATALOV	–	USSR

1. OPERATING CONDITIONS AND PROPOSED CONCEPTS

1.1. Operating conditions

The divertor is the exhaust system for the gaseous ashes of the fusion process and for the impurities resulting from plasma-wall interaction. In the reference design, the machine is equipped with a single-null divertor at the bottom of the plasma chamber.

The divertor operating conditions are given in Table VIII-1. The values estimated for particle and heat load to be extracted through the divertor are about 5.5×10^{23} parts/s and 80 MW. The absorption of this high heat flux in the divertor and the erosion due to the particle flux are the most severe problems to be solved. Under these conditions, some essential parts of the divertor collector plates will be damaged rapidly.

The design, therefore, has to provide for a rather frequent exchange of the divertor plates. The design effort has focused on developing solutions which minimize the amount of radioactive waste and allow an easy and rapid exchange of the divertor.

Other problems in the divertor region are:

- radiation damage of the supporting elements
- deposition of eroded materials from the first wall
- permeation of tritium to the coolant
- heat and particle load on the channel walls.

TABLE VIII-1. DIVERTOR OPERATING CONDITIONS

Total energy to divertor		80 MW
Divertor plate		
Ion energy		35 MW
Electron energy		35 MW
Ion flux		5.5×10^{23} s^{-1}
Average energy of ions		400 eV
Composition of ions		47% T, 47% D, 5% He, 0.5% C, 0.5% O
Neutral gas density at front of divertor plates		10^{19} m^{-3}
Peak energy flux to divertor plates normal to separatrix		
	outboard	8 MW/m^2
	inboard	4 MW/m^2
Peak ion flux to divertor plates perpendicular to separatrix		
	outboard	6×10^{22} $m^{-2} \cdot s^{-1}$
	inboard	3×10^{22} $m^{-2} \cdot s^{-1}$
Inclination of divertor plate to separatrix	outboard	14.5°
	inboard	30°
Divertor throat and channel walls		
Total energy		10 MW
Charge-exchange neutrals		5 MW
Radiation		5 MW
Total neutral flux		1.6×10^{23} s^{-1}
Average energy of neutrals		200 eV
Peaking factor of flux		2
Area on which the neutrals impinge		33 m^2
Five strips of 0.2 m length each, four of them adjacent to the ends of the divertor plates and the fifth on the wall facing the outside divertor plate		

FIG. VIII-1. F
of the inner an

The distributions of heat and particle fluxes on the two divertor plates are shown in Fig.VIII-1 for plates perpendicular to the separatrix. Since it would be extremely difficult to find satisfactory solutions under these conditions, the plates must be tilted against the incoming particle and heat flux. The geometry of the divertor region is given in Fig.VIII-2; Figs VIII-3 and VIII-4 show the distribution

FI

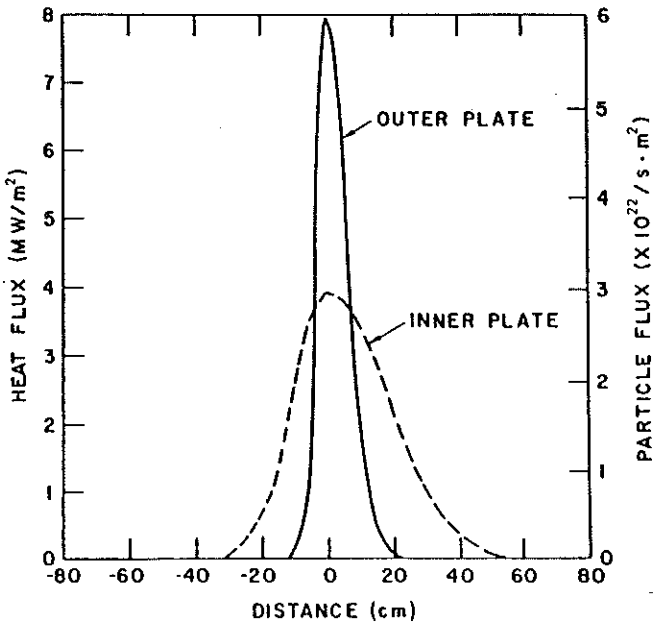

FIG. VIII-1. Heat and particle flux distribution perpendicular to the separatrix at the location of the inner and outer collector plates.

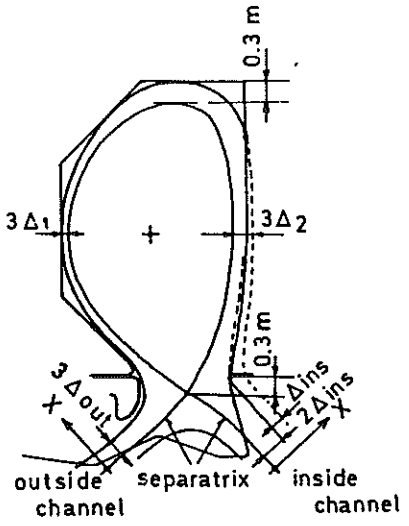

FIG. VIII-2. Cross-section through plasma chamber and poloidal divertor.

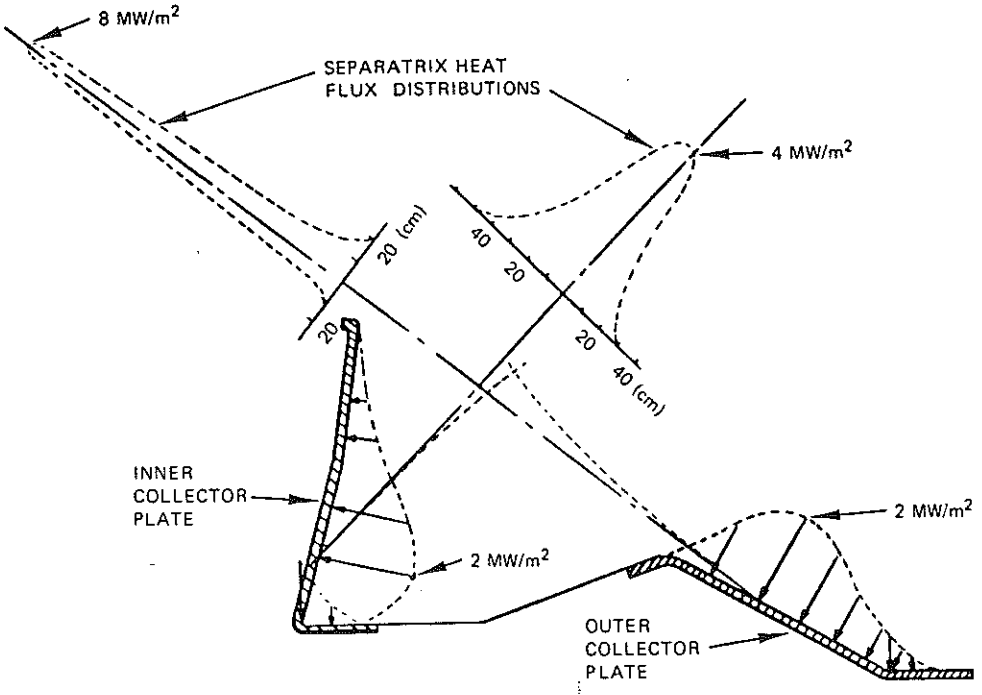

FIG. VIII-3. Heat flux distribution on divertor plates.

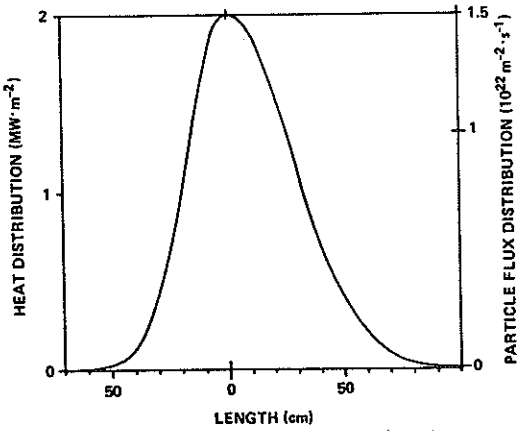

FIG. VIII-4. Heat and particle flux distribution on inclined inner and outer plates.

of heat and particle fluxes on perpendicular and inclined plates. The angle between plate and separatrix is 30° for the inner plate and 14.5° for the outer one. Under these geometrical conditions, the maximum heat flux is 2 MW/m^2 on both plates.

1.2. Proposed design concepts for the divertor plate

An examination of the divertor made it clear that viable designs must have several basic features. First, the problem of surface erosion has to be separated from the cooling problem. Therefore, all design solutions employ a high-efficiency heat sink protected by an armour with a low sputtering coefficient. Even under these conditions, however, it will be necessary to exchange the divertor several times because of the high calculated sputtering rates.

From sputtering data available in the literature it appears that the high-Z refractory metals have by far the lowest sputtering coefficients. For the INTOR divertor, tungsten and the molybdenum alloy ZM-6 have been considered as materials for the protective armour. The use of these metals includes a number of difficulties, for example embrittlement due to recrystallization at high temperatures and due to irradiation, and fabrication problems (machining, welding, etc.). Considering the large surface of the divertor plates (75 m^2), the production of the necessary materials and the overall weight (28 t) could also be significant problems.

A second common feature of the design solutions considered is the idea to incline the divertor plate with respect to the direction of the incoming heat and particle fluxes. This gives the advantage of a reduction of the specific heat and particle loads; however, the surface area of the divertor plates has to be increased by a factor of 2 to 4. A further difficulty resulting from the inclination is the necessity to carefully align the different elements of the plates in order to avoid hot spots with exceptionally high temperatures and erosion rates.

Because of the high heat flux on the divertor plates, it is important to consider thermal stresses. Their variation with the frequency of the burn cycles adds a fatigue problem. Thermal stresses will occur across the armour plate owing to the temperature gradient. If the armour is brazed to the heat sink, additional stresses will occur at the joints between both, owing to the differences in thermophysical properties such as the thermal expansion coefficients.

Two concepts for the construction of the divertor plates have been envisaged. The first, called the brazed concept, employs a braze material to join the protection armour plate to the heat sink, ensuring good heat conduction between armour and heat sink (see Fig.VIII-5).

The advantages of this concept are:

(a) A rather low collector plate temperature (the tungsten tiles will be kept below 450°C). In this case, no recrystallization takes place.
(b) Vaporization of oxide is kept low.

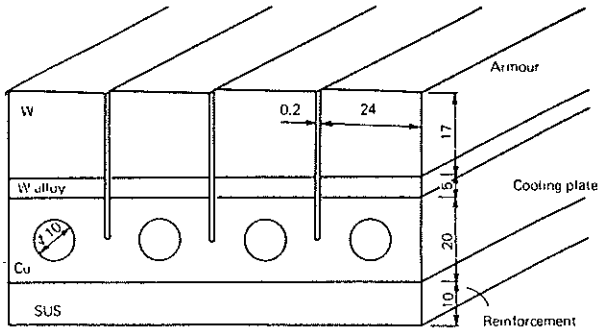

FIG. VIII-5. Brazed divertor plate concept. (Dimensions in mm)

The drawbacks of the brazed divertor plate are:

(a) High thermal stresses in the plate and on the interfaces between the different materials. No data exist on the fatigue behaviour of the brazes.
(b) Protection plate and copper heat sink will embrittle under fast neutron irradiation.

For this concept, the maximum lifetime is given by the erosion of the protection plate and is roughly 2 years. However, the fatigue properties of the braze and the heat sink may be more limiting than the sputtering erosion.

A modification of the brazed concept can be obtained by replacing tungsten for the protection plate by ZM-6, a molybdenum alloy, and copper for the heat sink by Zircaloy [5].

In order to reduce the problems resulting from the thermal stresses, the armour plate can be cut into small pieces (tiles). This procedure reduces the overall stresses, but introduces local stresses at the edges of the armour tiles. Another benefit of the tile approach is that the eddy currents generated in the divertor plates during disruptions are smaller and hence the forces on the divertor are strongly reduced. On the other hand, precise mounting of the pieces is required.

The second concept, which is called the mechanically attached concept, keeps the heat sink and protection plate structurally separated. In this concept, the thermal stresses at the interface are avoided. The protection plate is mounted in such a way that it can expand and bend freely as the temperature increases and therefore experiences only small thermal stresses. The plate itself is mainly cooled by emission of infra-red radiation (Fig. VIII-6).

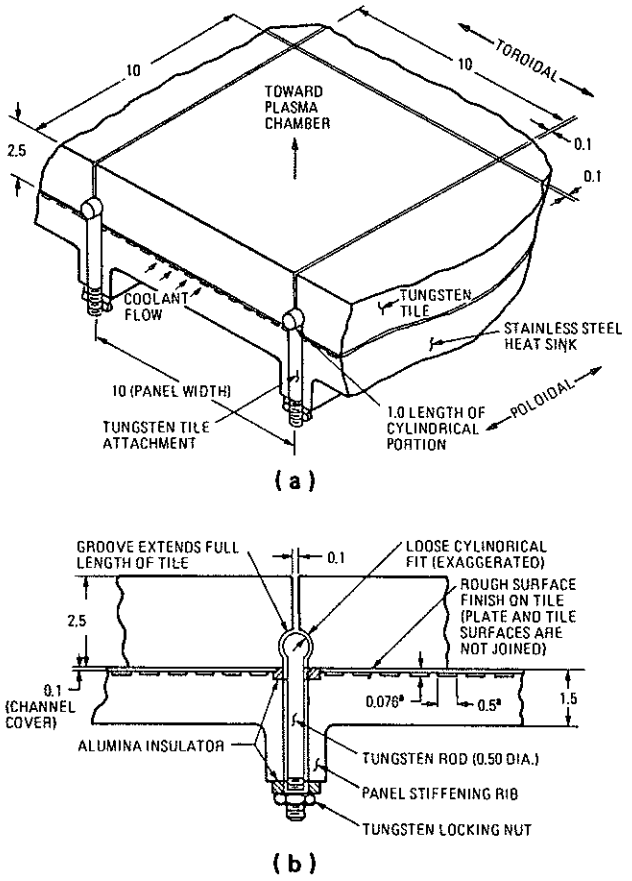

FIG. VIII-6. Mechanically attached divertor plate concept.
(a) Isometric cut-away through typical plate assembly
(b) Cross-section through typical plate assembly (looking in poloidal direction).
(All dimensions in cm; all dimensions are typical.)

[a] *Channel dimensions shown are for peak heat flux region only.*

The advantages of this concept are:

(a) Low thermal stresses in the protection plate.
(b) The heat sink is made of stainless steel, for which there exists a large data base on radiation damage, which allows to make more precise predictions of the lifetime of the structure.
(c) Possible re-use of the heat sink structure.

The disadvantages of this concept are:

(a) The tiles are heated to high temperatures (2350–2500°C) at which the tungsten will recrystallize. Recrystallized tungsten is brittle at low temperature.
(b) The erosion of the tiles may be enhanced by chemical sputtering.

The maximum lifetime of the divertor of this concept is determined by the erosion of the protection plate, as in the case of the first concept.

Both solutions lead to a partially exposed structure. It must still be determined to what extent charge-exchange high-energy neutrals may penetrate between the protective tiles and erode the base structure of the divertor by sputtering.

2. MATERIALS ASSESSMENT

In the two design concepts, several materials have been examined. Tungsten and ZM-6, a molybdenum alloy containing 0.1 to 0.2% Zr, have been used as protection materials, while stainless steel,copper and Zircaloy have been selected as heat sink structural materials. In this section, the properties of the candidate materials are presented and their sputtering behaviour, oxidation and radiation damage are discussed.

2.1. Thermophysical and mechanical properties

2.1.1. Tungsten

Values for the thermophysical properties of tungsten are presented in Table VIII-2, and some mechanical properties of tungsten are given in Tables VIII-3 and VIII-4.

Values for the infra-red emissivity are needed in order to calculate the temperature of the armour plate for the mechanically attached concept. Table VIII-5 gives the total emissivity of a clean plate tungsten surface. By increasing the surface roughness or by covering the surface with oxides, the emissivity of metals can be increased. Since tungsten oxide is volatile at high temperatures, the only means of increasing the emissivity of tungsten is to increase the surface roughness. For example, the surface can be roughened by sand-blasting. However, care has to be taken that the wavelength of the roughness is larger than the wavelength of infra-red radiation. Typically, at 3000 K the wavelength of maximum radiation is 1 μm. Roughness created by sputtering is probably much smaller than 1 μm Therefore, the emissivity values for the front side of the divertor plate may be close to the values given in Table VIII-5.

TABLE VIII-2. THERMOPHYSICAL PROPERTIES OF TUNGSTEN

Property		273 K	773 K	1273 K	1773 K	2273 K
Thermal expansion	(10^{-6} K^{-1})	4.4	4.5	4.7	5	5.4
Specific heat	(J/kg · K)	134	142	151	160	168
Thermal conductivity	(W/m · K)	144	128	113	106	102
Young's modulus	(GPa)	400	382	362	331	290
Poisson's ratio		0.31				
Melting point		3683 K				
Recrystallization temperature		1500 K				
Ductile-to-brittle transition temperature		398 K (cold-rolled) 588 K (recrystallized)				

TABLE VIII-3. TENSILE PROPERTIES OF RECRYSTALLIZED TUNGSTEN

Temperature (°C)	Total elongation (%)	Ultimate strength (MPa)	Yield strength (MPa)
0	0	750	750
250	6	550	250
500	61	350	145
750	57	275	105
1000	54	235	85
1250	49	185	70
1500	42	145	60
1750	32	105	45
2000	21	65	35

TABLE VIII-4. CREEP RUPTURE STRESSES (MPa) FOR PURE TUNGSTEN

Temperature (°C)	Lifetime		
	10 h	100 h	1000 h
1400	135	69	41
1600	58	38	25
1800	31	22	16
2000	19.5	13	9
2200	17	10	5.5

TABLE VIII-5. TOTAL EMISSIVITY OF TUNGSTEN

Temperature	500 K	1000 K	1500 K	2000 K	2500 K	3000 K
Emissivity	0.053	0.114	0.192	0.260	0.303	0.334

TABLE VIII-6. THERMOPHYSICAL PROPERTIES OF MOLYBDENUM

Property		273 K	773 K	1273 K	1773 K	2273 K
Thermal expansion	(10^{-6} K^{-1})	5.4	5.6	6.0	6.5	7.2
Specific heat	(J/kg · K)	251	251	310	370	460
Thermal conductivity	(W/m · K)	147	126	105	84	70
Young's modulus	(GPa)	300				
Poisson's ratio			0.32			
Melting point			2883 K			
Recrystallization temperature			1470 K			
Ductile-to-brittle transition temperature			273 K (recrystallized)			

TABLE VIII-7. MECHANICAL PROPERTIES OF WROUGHT MOLYBDENUM

Temperature (°C)	Ultimate tensile strength (MPa)	Yield stress (MPa)
0	1103	896
500	896	758
1000	790	690
1500	270	172

TABLE VIII-8. THERMOPHYSICAL PROPERTIES OF ZM-6

Thermal expansion	7×10^{-6} K^{-1}
Specific heat	251 J/kg · K
Thermal conductivity	120 W/m · K
Young's modulus	306 GPa
Ultimate strength	720 MPa

TABLE VIII-9. PROPERTIES OF HEAT SINK MATERIALS

Property		AISI 316		Zr – 2.5 Nb (annealed)		CDA copper 109	
		373 K	500 K	373 K	500 K	373 K	500 K
Thermal expansion	(10^{-6} K^{-1})	15	17	6.3	6.5	17	17.6
Specific heat	(J/kg · K)	470	540	300	310	390	420
Thermal conductivity	(W/m · K)	14	17	10	9.9	390	380
Young's modulus	(GPa)	197	178	79	69	120	110
Ultimate strength	(MPa)	560	450	593	441	220	190
Yield strength	(MPa)	230	150	462	345	70	–
Total elongation	(%)	60	40	17	18	55	–
Fatigue limit ($N = 10^5$)	(MPa)	300	250	310	240	110	–

TABLE VIII-10. TOTAL HEMISPHERICAL EMISSIVITY OF STAINLESS STEEL AT 300°C

Emissivity	Treatment
0.20	Optically polished
0.64	Polished and oxidized at 1173 K for 60 min
0.47	Polished, then shot-blasted
0.53	Shot-blasted, then oxidized at 923 K for 60 min
0.78	Shot-blasted, then oxidized at 1173 K for 180 min

On the more protected back-side, geometrical measures to increase the emissivity can be applied more successfully. Such measures can increase the emissivity by up to a factor of 2.

2.1.2. Molybdenum

The thermophysical properties and some mechanical properties of molybdenum are given in Tables VIII-6 and VIII-7. The total emissivity of molybdenum is about the same as that of tungsten. However, because of the much lower melting point of molybdenum, its use in the mechanically attached concept is not advisable. Some thermophysical properties of ZM-6 are given in Table VIII-8.

2.1.3. Heat sink materials

For the heat sink, stainless steel, copper and zirconium alloys have been considered. Stainless steel has the advantage that a rather large data base on irradiation behaviour exists. The lower electrical conductivity of stainless steel and Zircaloy reduces the eddy currents and electromagnetic forces induced during disruptions in the divertor structure. However, their poor thermophysical properties are a drawback with respect to temperature gradients and fatigue stresses. The different properties of the heat sink materials are listed in Table VIII-9.

For the mechanically attached divertor plate, the radiation properties of the materials are important for the calculation of the plate temperature.

The emissivity of stainless steel varies strongly with surface treatment. Table VIII-10 gives an example of possible variations of the emissivity after different treatments of stainless steel.

2.2. Changes of mechanical properties due to irradiation

The data base available for the different materials employed for the divertor design varies strongly. A large data base exists for stainless steel; these data are reported in Chapter VII. For tungsten and molybdenum, however, only a small amount of data is available. Even if the divertor plates are exchanged several times during the reactor lifetime, the fluences accumulated in the different parts will reach values of $\sim 10^{25}$ n/m^2. At these fluences, most metals have already undergone substantial changes in their mechanical properties. In general, with increasing fluence the yield stress and ultimate tensile stress increase and the ductility decreases.

2.2.1. Tungsten

Swelling after a radiation dose producing 9 displacements per atom (dpa) has been observed to be 1.5%, with the peak swelling temperature at 800°C. At 350°C the formation of void lattices has been observed. Neutron irradiation at 375°C up to 4 dpa in wrought material resulted in an increase of the yield stress by 50%, and the ductile-to-brittle transition temperature (DBTT) was then shifted from 125 to 375°C. Radiation effects anneal out at temperatures higher than 1000°C.

2.2.2. Molybdenum

The most important change for refractory metals due to irradiation is the shift in DBTT, which is about 200°C higher in molybdenum at 6×10^{25} n/m^2. Yield and ultimate stresses are increased by neutron irradiation.

2.2.3. Copper

Radiation damage has been studied extensively in pure copper. However, the tensile strength of pure copper is quite low. The use of cold-worked copper or copper alloys provides the necessary strength.

For annealed and cold-worked copper, data for the influence of neutron irradiation on the mechanical properties are available. In Figs VIII-7 to VIII-10 the changes of yield stress, ultimate tensile strength and ductility are given as a function of dose.

The rapid decrease in ductility with fluence is of concern. The thermal stresses generated by the high heat flux may introduce plastic deformations in the copper heat sink. The ductility appears to go to zero at about 2×10^{24} n/m^2. If this value is defined as the lifetime of the copper structure, then the copper lifetime is limited to about 3000 burn shots – an extremely short time. However,

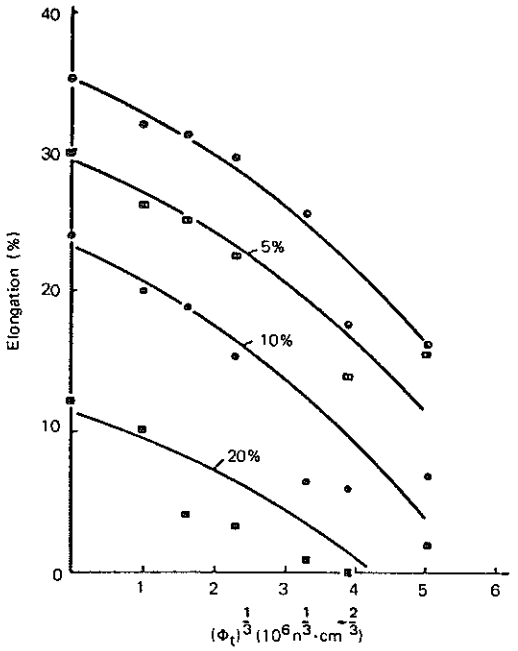

FIG. VIII-7. Effect of previous plastic deformation on the dose dependence of elongation before fracture of copper, tested at 20°C [9].

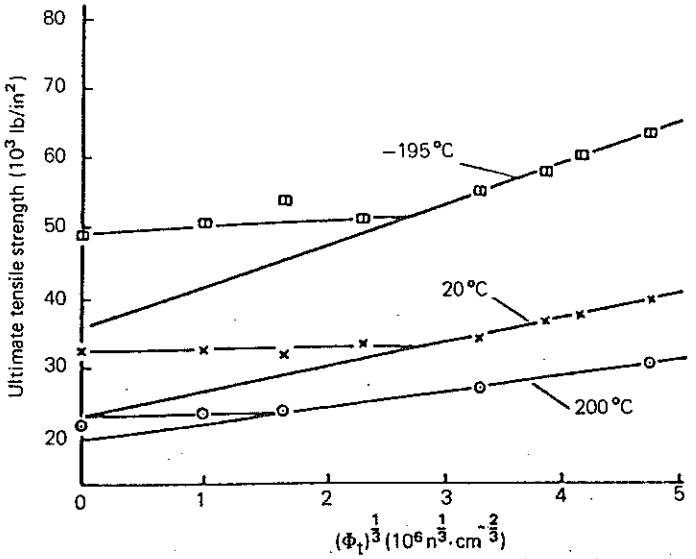

FIG. VIII-8. Ultimate tensile strength of polycrystalline copper at different testing temperatures.

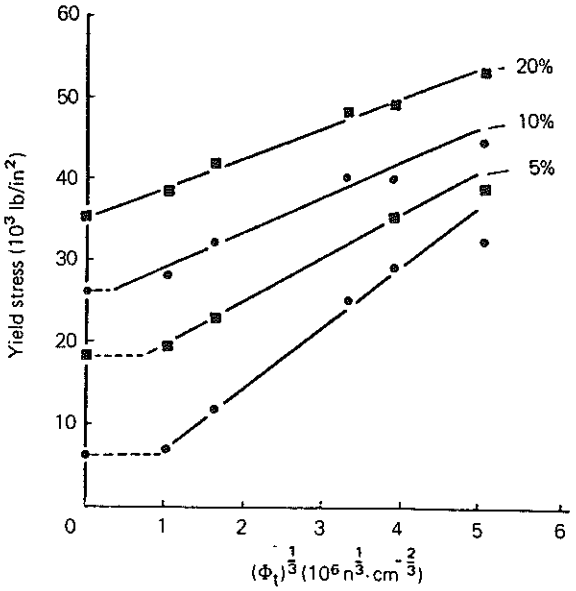

FIG. VIII-9. Lower yield stress of copper at 20°C as a function of (dose)$^{1/3}$ for specimens deformed to various degrees (neutron energies > 1 MeV).

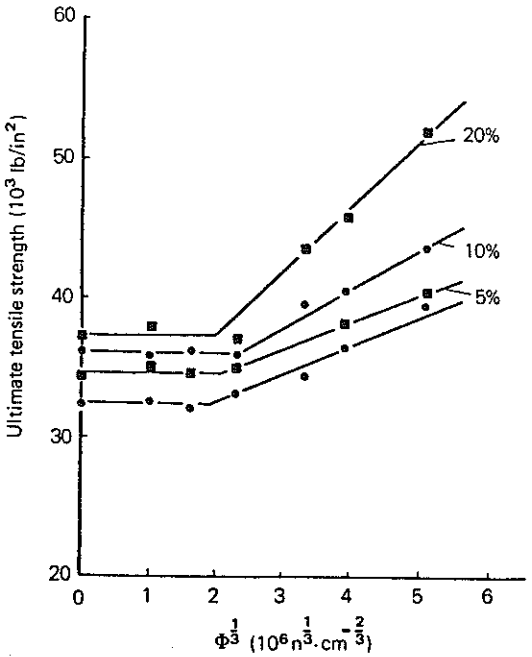

FIG. VIII-10. Ultimate tensile strength of copper at 20°C as a function of (dose)$^{1/3}$ for specimens deformed to various degrees.

the values presented are from experiments at room temperature. At higher temperatures, part of the radiation damage anneals out (Fig.VIII-8) and the lifetime of the copper structure may be longer. Additional investigations are necessary.

Swelling can probably be excluded as a problem, since the peak swelling temperature is 350°C [8] and the copper heat sink will always remain below this temperature.

2.2.4. Stainless steel

In the temperature range envisaged for the stainless steel heat sink, radiation damage is not expected to be a problem. More extensive data on stainless steel are given in Chapter VII.

2.3. Sputtering

The protection plates of the divertor and the surroundings of the channel are subjected to sputtering. Using values given in Table VIII-1, the peak fluxes on the inclined plates and the channel are:

Peak flux on the inclined plates	$1.5 \times 10^{22}\,m^{-2} \cdot s^{-1}$
Peak flux on the channel	$9.7 \times 10^{21}\,m^{-2} \cdot s^{-1}$

The self-sputtering on the divertor plates is taken into account by the following expression, which is a very rough approximation:

$$\eta_{eff} = \eta_{gas} \cdot \frac{1}{1 - \frac{1}{2}\eta_{self}}$$

In Table VIII-11, sputtering values for tungsten and ZM-6 are given. It is important to realize that the values for tritium are extrapolations and not measured values. Since tritium sputtering accounts for about 50% of the total sputtering, the effective sputtering coefficient is affected by an uncertainty of about 30%. The values for ZM-6 for the energies assumed in the INTOR design have been obtained by extrapolation of measurements made at 10 keV [6]. This extrapolation contains uncertainties which amount to a factor of 2 to 3 in the direction of higher values.

A much larger sputtering data base exists for molybdenum than for ZM-6. The sputtering rates for molybdenum are much higher than those cited in Table VIII-11 for ZM-6.

With the values stated in Table VIII-11, the divertor plate erosion can be calculated. The results are given in Tables VIII-12 and VIII-13. The sputtering erosion of the divertor plate is shown in Fig.VIII-11.

TABLE VIII-11. SPUTTERING COEFFICIENTS (atoms/ion)

400 eV		Tungsten [10]		ZM-6 [5]	
Ion	Composition	η	$\eta \cdot c$	η	$\eta \cdot c$
D	47%	4×10^{-4}	2.88×10^{-4}	2.4×10^{-4}	0.113×10^{-3}
T	47%	2×10^{-3}	0.99×10^{-3}	1.6×10^{-3}	0.75×10^{-3}
He	5%	7×10^{-3}	0.35×10^{-3}	8×10^{-3}	0.4×10^{-3}
C	0.5%	1×10^{-2}	0.05×10^{-3}	3×10^{-3}	0.15×10^{-3}
O	0.5%	2×10^{-2}	0.1×10^{-3}	5×10^{-2}	0.25×10^{-3}
Self-sputtering		0.5		0.6	
Effective sputtering			2.2×10^{-3}		2.4×10^{-3}

200 eV		Tungsten [10]	
Ion	Composition	η	$\eta \cdot c$
D	47%	5.6×10^{-5}	0.26×10^{-4}
T	47%	3×10^{-4}	1.41×10^{-4}
He	5%	1×10^{-3}	0.5×10^{-4}
C	0.5%	5×10^{-3}	0.25×10^{-4}
O	0.5%	1×10^{-2}	0.5×10^{-4}
Effective sputtering			2.92×10^{-4}

TABLE VIII-12. MAXIMUM DIVERTOR PLATE EROSION

Material	Erosion rate (mm/a)			Erosion over reactor life (mm)
	Stage I	Stage II	Stage III	
Tungsten	1.8	3.3	6.6	68.6
ZM-6	1.9	3.6	7.1	74.3

TABLE VIII-13. MAXIMUM CHANNEL EROSION

Material	Erosion rate (mm/a)			Erosion over reactor life (mm)
	Stage I	Stage II	Stage III	
Tungsten	0.152	0.28	0.56	6

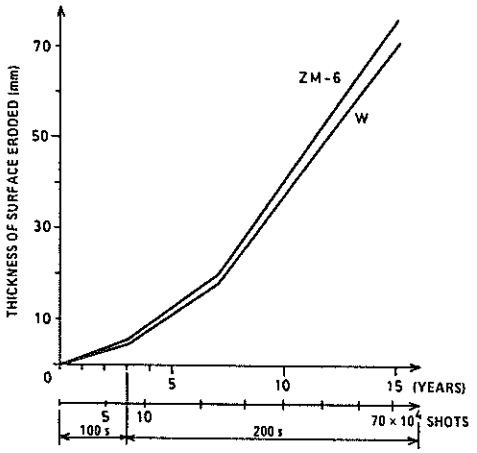

FIG. VIII-11. Sputtering erosion of tungsten and ZM-6 at the divertor operating conditions given in Table VIII-1.

2.4. Oxidation/chemical sputtering

The discharge gas coming to the divertor is assumed to contain ~ 0.5% impurities, which have been summarized as oxygen. If the whole amount is really oxygen, the following considerations on oxidation will apply. Both protection materials, tungsten and molybdenum, interact with oxygen and form volatile oxides. This oxidation is an additional erosion process which reduces the lifetime of the protection plate, especially at higher temperatures. Molybdenum is more affected by oxygen. Above 600°C the oxidation rate of molybdenum is 5–10 times faster than the oxidation rate of tungsten in a gaseous environment.

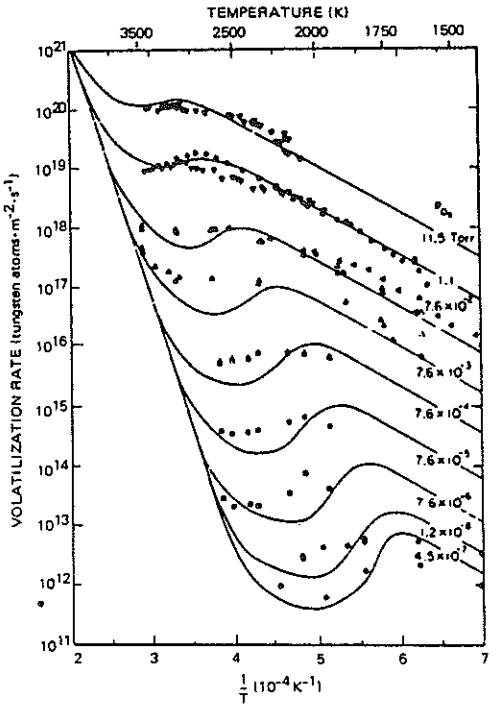

FIG. VIII-12. Tungsten oxidation rate at high temperature ($1400\ K < T < 3500\ K$) and low pressure (4.5×10^{-7} torr $\leq p < 11.5$ torr). The volatilization rate I_W is defined as the number of tungsten atoms removed from the surface per square centimetre per second by oxidation and sublimation [11].

The oxidation rate of tungsten in oxygen gas is represented in Fig.VIII-12 [11]. The situation for the operating conditions of INTOR is given by the solid line in Fig.VIII-13. However, this curve is valid only for the interaction of oxygen molecules with tungsten. In the case of the divertor plate, the oxygen is ionized, and the probability of ion adsorption on the surface is much greater than that of molecular adsorption. The resulting volatilization is predicted to be significantly greater for ionized oxygen, which is shown by the dotted line in Fig.VIII-13.

Under these conditions, the chemical sputtering by oxygen for temperatures below 2000 K is of the same magnitude as the physical sputtering. In the region around 2500 K, it is two orders of magnitude smaller, as shown in Fig.VIII-13.

Since the oxygen is ionized, oxidation and chemical sputtering of the surface of tungsten and molybdenum will also occur at temperatures as low as a few hundred degrees Celsius. The impact of this oxide on the physical sputtering rate must be considered in future analysis.

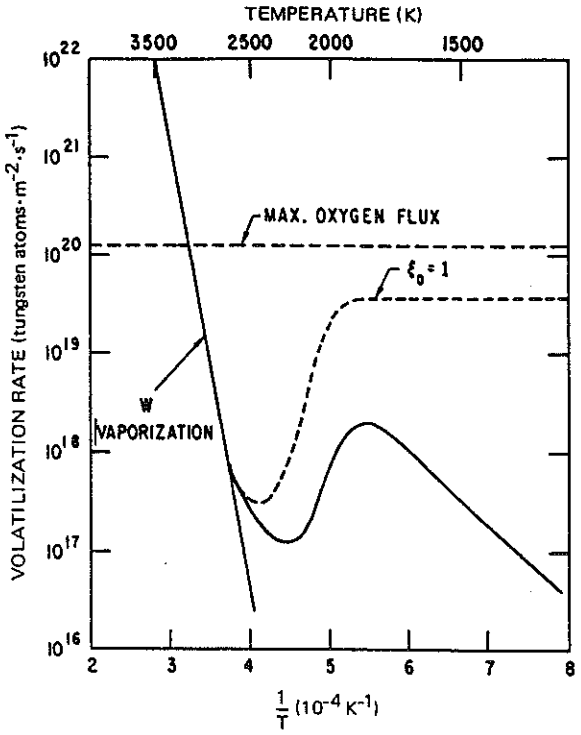

FIG. VIII-13. Predicted tungsten volatilization rate due to oxygen particle flux [4].

The results do not consider the possibility of recycling the oxygen between the WO_x in the gas phase in front of the divertor plate and the plate itself. To evaluate this possibility, it is necessary to know the cross-section for the ionization and dissociation of the different tungsten oxides.

3. NEUTRONICS ANALYSIS

Two divertor collector plate design concepts were analysed to determine the nuclear heating rate and the neutron damage in the tiles and the support material [4]. In both cases the tile material facing the plasma is tungsten. The support plate for the tiles is made of copper in the first design and of stainless steel in the second. Water is used in both design concepts to cool the support plate, while the tungsten tiles are passively cooled by radiation and conduction. The divertor

TABLE VIII-14. DIVERTOR COLLECTOR PLATE DIMENSIONS AND COMPOSITIONS USED IN THE NEUTRONICS ANALYSIS

Component	Thickness (cm)	Material
A. Divertor plate with copper support material		
Tile material	2.5	Tungsten
Support material	1.1	Copper
	0.65	Water (H_2O)
	1.65	Copper
B. Divertor plate with 316 stainless steel support material		
Tile material	2.5	Tungsten
Support material	0.2	316 SS
	0.65	Water (H_2O)
	0.65	316 SS

collector plate dimensions and compositions used in the neutronics analysis are listed in Table VIII-14 for both designs. The tungsten tiles are 2.5 cm thick in both cases. The support material is 3.2 cm and 1.5 cm thick, including the water coolant, for the copper and stainless steel design concepts, respectively.

Figures VIII-14 and VIII-15 give the spatial nuclear heating rates (per megawatt of neutron wall loading) for both designs. The heating rate in the tungsten tile material is dominated by gamma heating. The maximum nuclear heating rate in the tungsten tiles occurs at the back of the plate. The increased heating at the back of the plate is due to an increase in the low-energy neutron flux by reflection from the support material (copper or stainless steel), causing an increase in the (n,γ) reaction rate in the tungsten tiles. The ratio of maximum to minimum heating rate in the tungsten tiles is 1.65 for copper and 1.39 for stainless steel. The nuclear heating in the stainless steel support material is 15% less than in copper. The nuclear heating in molybdenum is about 75% of the heating in tungsten.

The results of these calculations may be taken as an indication of the heating rates that can be expected, since the exact values depend rather strongly on the overall design and can be calculated only when the design is fully established.

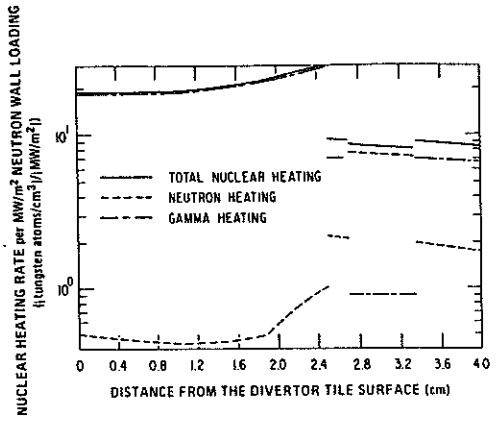

FIG. VIII-14. Spatial nuclear heating rates in the design concept of the divertor collector plate with stainless steel support material for the tile [4]. —— total nuclear heating, – – – neutron heating, –·–·– gamma heating.

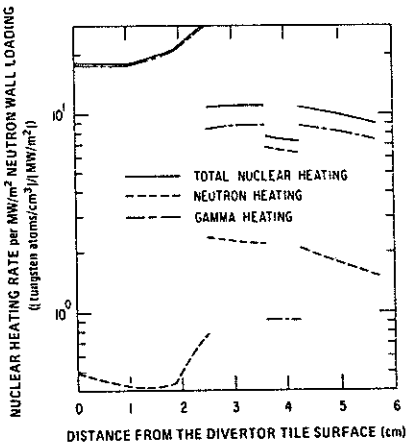

FIG. VIII-15. Spatial nuclear heating rates in the design concept of the divertor collector plate with copper support material for the tile [4]. —— total nuclear heating, – – – neutron heating, –·–·– gamma heating.

The maximum helium production rate is 71 and 43 ppm (at.) per MW·a/m² in copper and stainless steel, respectively. However, the hydrogen production rates are about the same for both designs. The gas production rates in the tungsten tiles are 3 ppm (at.) for He and 9 ppm (at.) for H per MW·a/m². The maximum displacement rates are 10, 3 and 7 displacements per atom (dpa) per MW·a/m² for copper, tungsten and stainless steel, respectively.

4. THERMOHYDRAULIC ANALYSIS

4.1. Cooling system

4.1.1. Heat loads

The divertor collector plates are cooled with water. The cooling system has to extract the power transported by the ions and electrons, which is about 80 MW (Table VIII-1), and the heat generated in the protection plates and in the cooling plate itself.

Assuming 2 cm of tungsten covering about 75 m^2 surface area, the heat generated is about 30 MW in the tungsten armour and approximately 10 MW in the cooling plate. Altogether, the cooling system must be designed for 120 MW. The maximum specific heat flux will be 2.5 MW/m^2 for the brazed concept, composed of 2 MW/m^2 from conduction (as explained in Fig.VIII-3) and 0.5 MW/m^2 from neutrons and photons. The contribution from the photons is design-dependent, as it comes from the structure behind the tiles and other parts of the reactor system.

For the mechanically attached concept, the heat coming from the armour plate is about 1.2 MW/m^2. Thus the total load is 60 MW in the heat sink and the peak flux is 1.3 MW/m^2. The temperature distribution varies with the periodicity of the burn cycle (see Table VIII-18). For the material and the thickness involved, the time constant is about 30 s. This time constant can be expected also for the brazed version. Another variation is the gradual erosion of the tiles, especially in the region of peak ion flux. Because of erosion, the temperature of the tile surface will decrease with operation time.

The brazed multi-layer structure has cooling channels in the copper heat sink, with a diameter of 10 mm, spaced 24 mm apart. The structure is shown in Fig.VIII-5. In the case of the mechanically attached concept, the structure below the tiles is made of stainless steel (Fig.VIII-16). The cooling channels are about 5 mm by 0.76 mm in cross-section, with a spacing of 7 mm.

The cooling must be accomplished without boiling in order to avoid instabilities of the flow distribution in the parallel cooling channels. Indeed, the pressure drop over these channels is constant and it is not changed if the flow in one of the channels is reduced by some disturbance. Therefore, if local boiling starts in one tube, the friction increases and the flow will drop more, with the result that overheating or burnout takes place. The neighbouring channels will then also come to the burnout condition because the heat flux will increase by 50%.

Design parameters for cooling without local boiling are presented in Table VIII-15 for both the brazed and the mechanically attached concepts. The design velocity of the water flow is taken 30% higher than the minimum velocity connected with the design inlet pressure. The pressure prevents boiling at the wall in the peak flux region for this minimum velocity.

TABLE VIII-15. DESIGN PARAMETERS FOR COOLING WITHOUT LOCAL BOILING[a]

	Heat sink	
	Brazed concept	Mechanically attached concept
Heat load by conduction and convection	80 MW	–
Heat load by radiation and neutrons	40 MW	–
Heat load, total	120 MW	60 MW[b]
Peak heat flux by ions and electrons	2.0 MW/m^2	–
Heat flux by radiation and neutrons	0.5 MW/m^2	–
Peak heat flux on plate	2.5 MW/m^2	1.2 MW/m^2 [b]
Peak heat flux on cooling channel	8 MW/m^2	1.7 MW/m^2
Number of cooling channels	2320	8286
Shape and dimension	10 mm	5 mm × 0.76 mm
Channel length	1.3 m	1.3 m
T_{in}	50°C	50°C
Velocity	13 m/s	8 m/s
Heat transfer coefficient	7.2×10^4 W/m·K	6×10^4 W/m·K
$T_{wall} - T_{mix}$	111 K	28 K
$T_{in} - T_{out}$	13 K	59 K
T_{out}	63°C	109°C
T_{wall}	175°C	137°C
P_{out}	16 bar	6.8 bar
$P_{in} - P_{out}$	2.3 bar	7.2 bar
P_{in}	18.3 bar	14.0 bar
Mass flow	2300 kg/s	240 kg/s
Pumping power	0.54 MW	0.18 MW
Minimum velocity without local boiling	10 m/s	6 m/s
T_{wall} at minimum velocity	201°C	163°C

[a] Conditions in heat sink at point of peak heat load.
[b] Half of brazed version.

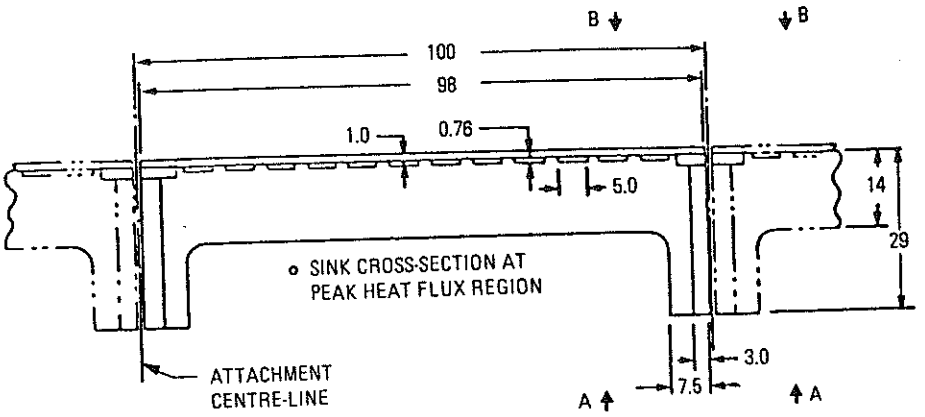

FIG. VIII-16. Cooling plate for radiation-cooled tiles [4]. (All dimensions in mm)

4.2. Temperature profiles in the armour and heat sink

4.2.1. Brazed concept

For this concept the calculation of temperature is quite straightforward. The only deviations from isotherms parallel to the plane of the tiles will be found in the region of the cooling channels, where the exact form of the isotherms will depend on the diameters and spacing of the cooling channels. For a multi-layer brazed (Elconite braze) structure of tungsten and copper, the surface temperature of the protective tiles will be 400°C (see Fig.VIII-17).

For a combination of 20 mm molybdenum with 4 mm Zircaloy, the surface temperature will be 800°C (Fig.VIII-18). The temperature difference between the surface and coolant-channel wall for the two cases is 280°C and 700°C, respectively.

4.2.2. Mechanically attached concept

The temperature of the armour plate is strongly influenced by the choice of the radiation parameters. These are the emissivity of the back and front of the tungsten tiles, the emissivity of the stainless steel at the heat sink and on the other surfaces, and the viewing factor for the tiles. It can be assumed that the emissivity can be increased on those surfaces which are protected from sputtering. It is doubtful whether this is possible on those surfaces which are constantly eroded by sputtering. Increases in emissivity to much above that of the bare metal are unlikely if the tile front surface becomes smooth owing to sputtering.

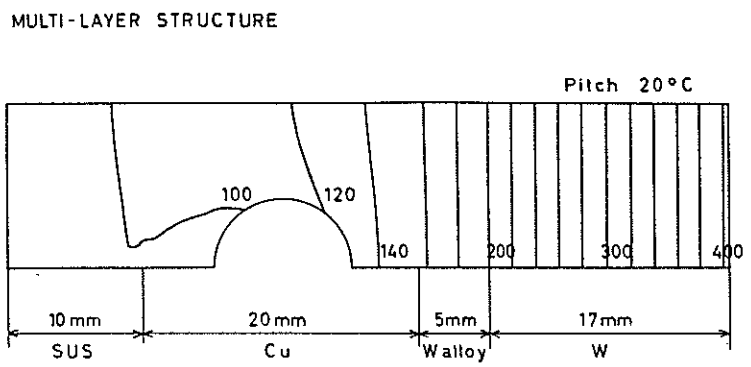

FIG. VIII-17. Temperature profile in a divertor plate obtained by finite-element calculations for 2 MW/m² and thermal conductivity of 167 and 230 W/m · K for tungsten and tungsten alloy, respectively.

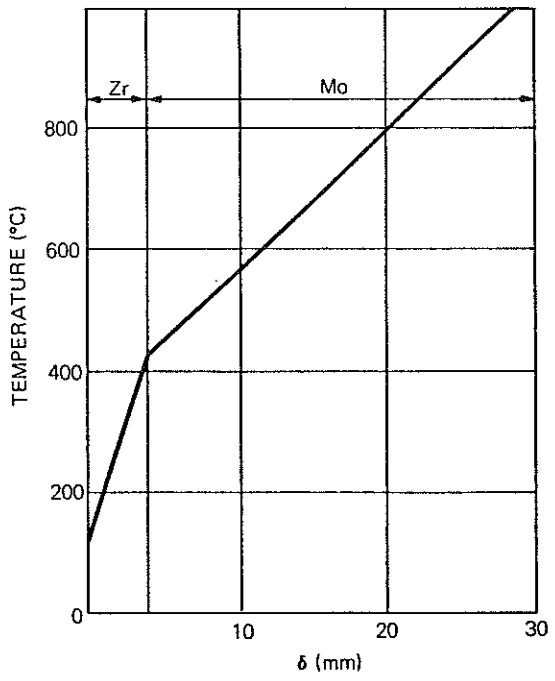

FIG. VIII-18. Temperature distribution over a 20 mm Mo/4 mm Zircaloy plate for 2 MW/m² [3].

TABLE
TEMPEI

Tungsten
TS[a]
1.0
0.7
0.6
0.5
0.4
0.3
1.0
1.0
1.0
1.0
1.0
1.0
1.0
1.0
0.8
0.7
0.6
0.5
0.3
0.6
0.5
0.4
0.3
0.6
0.6
0.5
0.4

a TS =
b BS =
c Selec

TABLE VIII-16. PARAMETRIC ANALYSIS OF TUNGSTEN TILE TEMPERATURES

Tungsten emissivity		SS emissivity		Viewing factor	Tile temperature (K)	
TS[a]	BS[b]	Chamber	Heat sink		TS[a]	BS[b]
1.0	1.0	1.0	1.0	1.0	2287	2062
0.7	0.7	1.0	1.0	1.0	2490	2259
0.6	0.6	1.0	1.0	1.0	2583	2350
0.5	0.5	1.0	1.0	1.0	2698	2462
0.4	0.4	1.0	1.0	1.0	2846	2606
0.3	0.3	1.0	1.0	1.0	3051	2806
1.0	1.0	0.8	0.8	1.0	2412	2182
1.0	1.0	0.6	0.6	1.0	2583	2350
1.0	1.0	0.5	0.5	1.0	2698	2462
1.0	1.0	0.4	0.4	1.0	2846	2606
1.0	1.0	0.5	0.5	0.8	2621	2411
1.0	1.0	0.5	0.5	0.6	2556	2366
1.0	1.0	0.5	0.5	0.4	2497	2324
1.0	1.0	0.5	0.5	0.2	2445	2286
0.8	0.8	0.8	0.8	0.5	2481	2263
0.7	0.7	0.7	0.7	0.5	2590	2377
0.6	0.6	0.8	0.8	0.25	2626	2406[c]
0.5	0.5	0.8	0.8	0.25	2734	2510
0.3	0.3	0.5	0.5	0.25	3136	2921
0.6	0.7	0.7	0.9	0.25	2583	2333
0.5	0.7	0.7	0.9	0.25	2649	2372
0.4	0.7	0.7	0.9	0.25	2725	2415
0.3	0.7	0.7	0.9	0.25	2816	2464
0.6	0.7	0.6	0.9	0.25	2590	2337
0.6	0.7	0.4	0.9	0.25	2604	2345
0.5	0.6	0.5	0.9	0.25	2697	2435
0.4	0.6	0.5	0.9	0.25	2776	2481

[a] TS = top surface.
[b] BS = back surface.
[c] Selected for two-dimensional analysis.

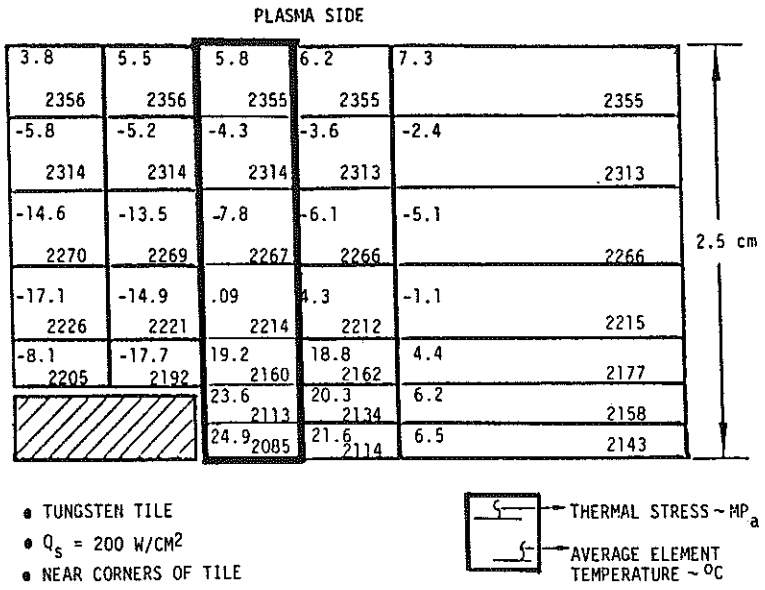

FIG. VIII-19. Estimated stresses and temperature of divertor collector tiles for the mechanically attached concept [4].

TABLE VIII-17. REFERENCE PARAMETERS FOR TWO-DIMENSIONAL TRANSIENT ANALYSIS

Surface heat flux	2 MW/m^2
Neutron heating rate	18 MW/m^3
Tile thickness	25 mm
Tile width	100 mm
Heat sink material	Austenitic stainless steel
Heat sink thickness	15 mm
Heat sink top skin thickness	0.75 mm
Coolant temperature (in/out)	50/100°C
Tile/heat-sink conductance	0 W/m^2 · K
Tile/attachment conductance	568 W/m^2 · K
Tungsten emissivity	0.6
Stainless steel emissivity	0.8
Viewing factor	0.25
Maximum surface temperature	2376°C
Maximum ΔT	320°C

TABLE VIII-18. TWO-DIMENSIONAL CALCULATION OF TRANSIENT TEMPERATURE (°C) FOR THE INITIAL BURN CYCLE

Node[a]	Time[b]					
	10 s	20 s	40 s	110 s	210 s	245 s
24	261	574	1197	2003	2085	1608
25	264	581	1208	2028	2113	1621
26	271	596	1230	2072	2160	1644
27	284	618	1261	2123	2214	1667
28	312	662	1310	2176	2267	1678
29	356	724	1374	2225	2313	1678
30	420	806	1453	2272	2355	1667

[a] Temperature positions: x = 6.25 mm
y = 24 – 15.75 mm, 25 – 17.25 mm, 26 – 19 mm, 27 – 22.5 mm, 28 – 27.5 mm, 29 – 32.5 mm, 30 – 37.5 mm.

[b] 10 s = begin of burn (end of start-up)
210 s = end of burn (begin of shut-down)
245 s = end of dwell.

Table VIII-16 gives the results of a one-dimensional parametric analysis of the temperature at the centre-line of a tungsten tile for different sets of emissivity values. For this analysis, no heat conduction is assumed to occur between the tiles and the heat sink. Assuming that the emissivity at the front side of the tiles can be raised to 0.6, the surface temperature will be ~2350°C. For emissivities of 0.3 at the front of the tiles, the surface temperature is 2500°C. By extrapolation, the maximum temperature difference between front and back surface is found to be 320°C at the end of the burn cycle. During the dwell time the back-surface temperature decreases to about 1600°C (Table VIII-18). Figure VIII-19 shows the two-dimensional temperature distribution for the end of the burn.

A two-dimensional model was also analysed for the conditions of Table VIII-17, in order to determine the temperature distribution near the mechanical attachment. The results are given in Table VIII-18.

5. STRESS ANALYSIS

Because of the temperature gradients in the armour plates and in the heat sinks, thermal stresses develop in both structures. In the case of the brazed concept, additional stresses appear through the braze, due to the differences in thermophysical properties (e.g. thermal expansion coefficient) between the protection plate and the heat sink.

5.1. Design for the brazed concept

The temperature gradient resulting from extraction of the entire heat load by the heat sink creates high thermal stresses. Stresses due to differences in thermal expansion between armour and sink have to be superimposed. Figure VIII-20 gives the results of finite-element stress calculations on a tungsten, tungsten-alloy, copper divertor plate (tungsten thickness 1.7 cm, heat flux 2 MW/m^2). The maximum stress values are 130 MPa and 110 MPa at the upper and lower interfaces.

5.2. Design for the mechanically attached concept

Because of the mounting method, which allows free rotation and bending of the tiles, the thermal stresses are much lower than for the brazed concept. A two-dimensional thermal stress model was constructed for a 25-mm-thick tile and the operating conditions given in Table VIII-17. Figure VIII-19 shows one half of a tile with a symmetric two-dimensional temperature distribution (the temperatures are for the end of the burn of 210 s). Temperature gradients near the tile corners are increased, owing to the additional heat flow through the attachments. The colder areas near the corners are stressed by the hotter bulk of the tile, which results in higher predicted stresses near the corners, as compared with the general stresses in the centre of the tile. The predicted stresses are below the yield strength of recrystallized tungsten at the relevant temperatures.

Figure VIII-21 presents the final thermal strain distributions of the row of elements outlined in Fig.VIII-19, at different times of the burn cycle. The final strains are linear and represent the conditions where the edges are allowed to rotate and expand freely. The stresses in the tile at any point are the result of the difference between the thermal strain and the final strain; this difference is called the mechanical strain, which actually produces stresses in the tile.

The mechanical strain on the elements actually changes sign over the burn cycle. Plastic straining does occur at various times during the initial cycles. The cooler region in the corner of the alumina insulator causes greater non-linearities in the temperature gradients and thus the highest stresses throughout the cycle were found in that region. A refinement of the analysis permitted the history

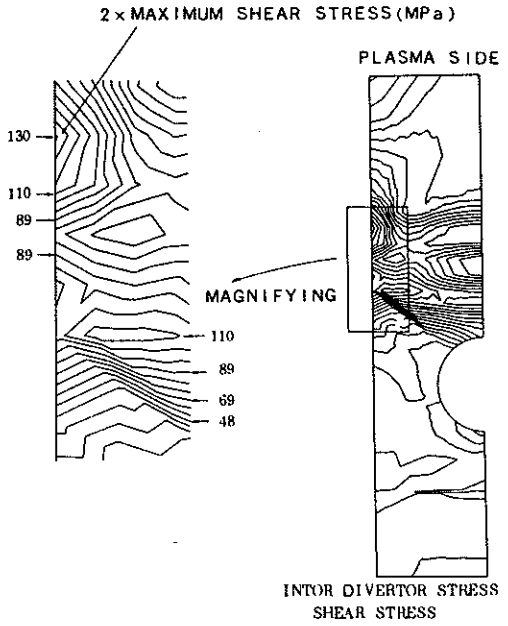

FIG. VIII-20. Stress distribution in a multi-layer divertor plate. The peak stresses appear at the interfaces between different materials.

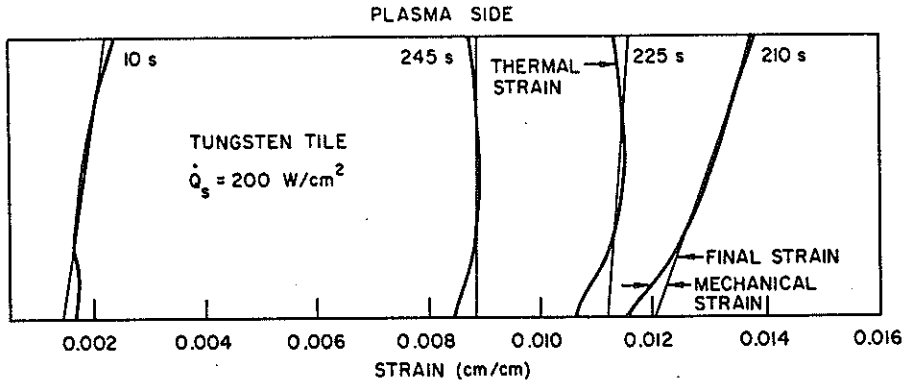

FIG. VIII-21. Strain distribution in one divertor collector plate tile over the thermal cycle [4].

of plastic strains on each element to be accounted for in determining the overall section response. The effect of accumulated plastic strains is clearly visible in the 245 s plot in Fig.VIII-21, the time point at which the stresses are highest. The calculated stresses and strains are all quite low. Therefore, the conclusion is that the stresses are in an acceptable range.

The stresses in the top skin of the heat sink are determined by the surface heat flux, the skin thickness, the water pressure and the amount of skin restraint. Analysis has shown [4] that, under the reference conditions, a stainless steel skin thickness of 1.75 mm or less will provide a heat sink lifetime greater than the reactor lifetime.

6. ELECTROMAGNETIC ANALYSIS

Electromagnetic forces on the divertor will be generated by the pulsed poloidal field coils or by disruptions. Estimates of the possible forces have been made for different geometries, for disruptions as well as for normal burn cycles. In general, the forces generated by the varying magnetic fields assumed are within the allowable limits. Detailed calculations are only possible for a definite design.

Figure VIII-22 gives sketches for two examples of divertor configurations, for which approximate calculations have been made.

For a panel such as in Fig.VIII-22(a), with dimensions of 1 m × 1 m, perpendicular to the pulsed field, a current of 120 A will be induced if it is made of stainless steel and of 5500 A if the material is copper. In a toroidal field of 6 T, for example, these currents will produce out-of-plane forces of 740 N and 33 000 N for the stainless steel and copper panel, respectively. In a 10 cm × 10 cm tungsten tile, the induced current will be 28 A, which will interact with the toroidal field to give an out-of-plane force of 17 N. The direction of the forces changes during the cycle.

In order to reduce the electromagnetic forces, it is likely that the divertor support will be a kind of frame structure as shown in Fig.VIII-22(b). Calculations performed for such a configuration, where the radial elements are copper tubes and the azimuthal elements are of stainless steel, give currents of about 260 A, which result in 2600 N/m in a toroidal field of 7.5 T. The individual protection plates are subjected to a torque stress, the magnitude of which has been calculated to be 37 MPa in the heat sink and 60 MPa in the stainless steel reinforcement [3, 4, 5].

7. LIFET

The fo
structure:

(a) Erosion
(b) Embritt
(c) Fatigue
(d) Embrit
(e) Fatigue

These pote
them is life

7.1. Erosic

Physi
and in Tab
Uncertaint
of 2–3 for
attached c
(dotted lin
about the
temperatu
The
at 50% av

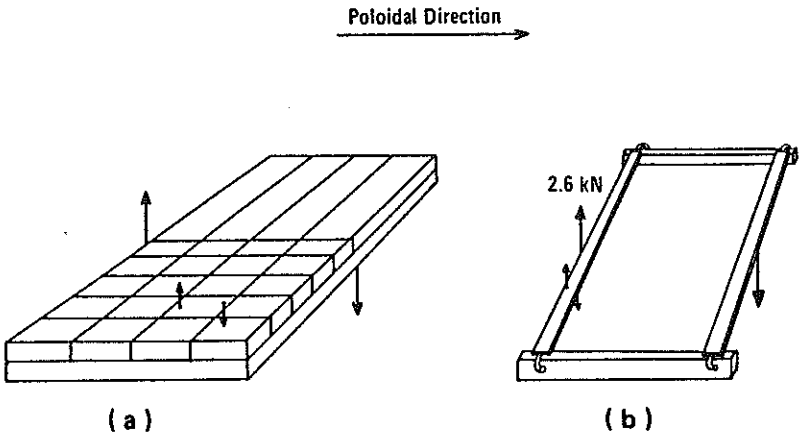

FIG. VIII-22. Schematic divertor plates for the calculation of electromagnetic forces.

7. LIFETIME EVALUATION

The following problems may limit the lifetime of the divertor plate and structure:

(a) Erosion of the divertor plate due to physical and chemical sputtering
(b) Embrittlement of the divertor plate due to recrystallization and irradiation damage
(c) Fatigue limits of the protection plate under cyclic thermal stresses
(d) Embrittlement of the heat sink under irradiation
(e) Fatigue limits of the heat sink.

These potential limitations are evaluated below, in order to determine which of them is lifetime-limiting on the basis of the available data.

7.1. Erosion of the divertor plate

Physical sputtering rates for different plate materials are given in Fig.VIII-11 and in Table VIII-12. Chemical sputtering is not considered in these values. Uncertainties in the sputtering coefficients are 50% for tungsten and a factor of 2–3 for ZM-6. Chemical sputtering will be important for the mechanically attached concepts. If the values given in Fig.VIII-13 are used for ionized oxygen (dotted line), then chemical sputtering is low in the centre of the plate and of about the same value as the physical sputtering at the outer parts where the plate temperature will be lower.

The maximum lifetime of a 2 cm tungsten plate is predicted to be ≅ 2 years at 50% availability or 150 000 burn-cycles (see Section 3.3).

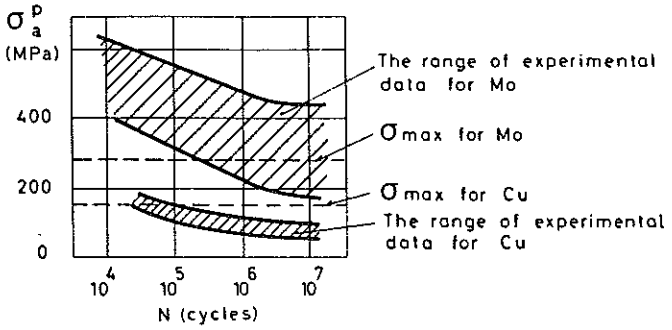

FIG. VIII-23. Fatigue curves of divertor materials: upper and lower limits of Mo and Cu. The dotted lines indicate the working stress of Mo and Cu in a brazed multi-layer plate [5].

7.2. Embrittlement of the divertor plate

Tungsten will recrystallize very rapidly at temperatures above 1500 K. It will therefore be brittle at low temperatures.

Embrittlement of the protection material is also caused by neutron irradiation. After 6×10^{25} n/m^2 the ductile-brittle transition temperature is shifted upward by about 200°C. This fluence corresponds to a radiation time of 1 year at 50% availability. In these cases the protection materials will be required to work in the brittle state when their temperature is below 350°C, as will be the case in the brazed concept during normal operation and in the mechanically attached concept at shut-down. In future, it must be evaluated to what extent brittleness will reduce the fatigue resistance of the divertor plates.

7.3. Fatigue limits of the protection plate

Fatigue data at high temperatures are available only for molybdenum. The fatigue curve given in Fig.VIII-23 is for unirradiated but embrittled material. The stress levels indicated in Fig.VIII-23 are for a 2-cm-thick tile of ZM-6 brazed onto a copper heat sink. These levels indicate that the fatigue life of the tiles would be considerably longer than 1 year. It must be pointed out, however, that irradiation effects are not considered here. They may have a severe impact on the predicted fatigue life.

7.4. Embrittlement of the heat sink

As pointed out in Section 2.2.3, embrittlement by neutron radiation of the copper heat sink is a serious problem, since it would limit the copper lifetime to

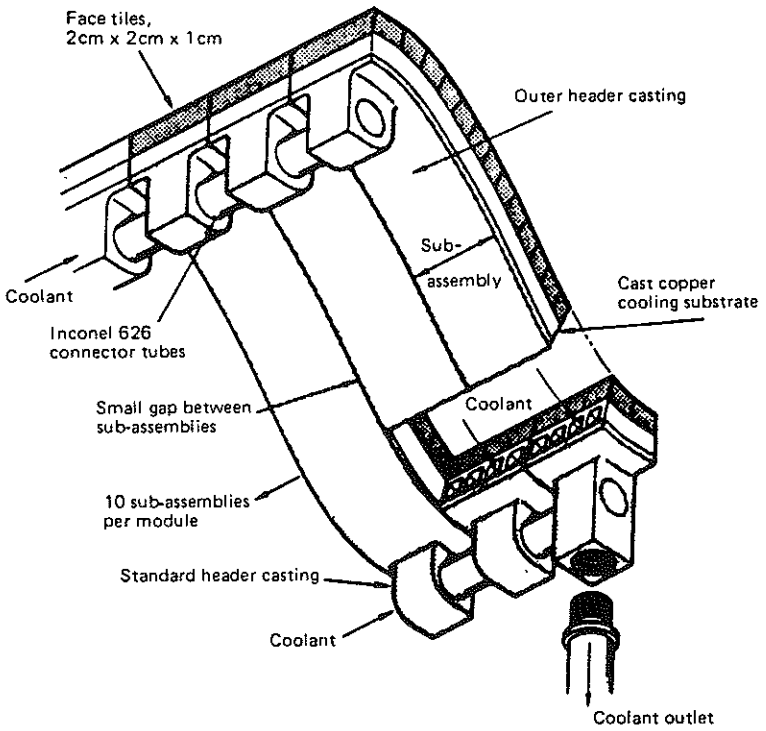

FIG. VIII-24. Example of the design of a multi-layer divertor plate with radial cooling channels [4].

considerably less than 1 year. For stainless steel heat sinks, this limit would be of the order of the reactor lifetime.

7.5. Fatigue limits of the heat sink

The fatigue limit of unirradiated copper is also given in Fig.VIII-21. According to the stress calculations for the brazed structure in Section 4.2, about 10^5 cycles are predicted for the lifetime of the device. Radiation may decrease the expected number of cycles.

For the stainless steel heat sink with a skin thickness of $\leqslant 1.75$ mm the fatigue limit for the unirradiated material would not be reached during the expected reactor lifetime. However, it should be mentioned that neutron irradiation embrittles steels and the associated weldments.

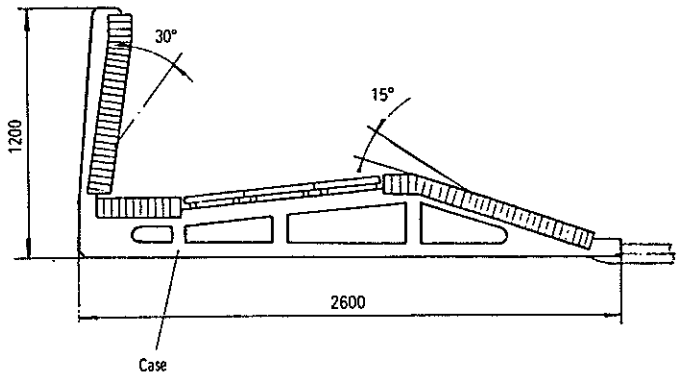

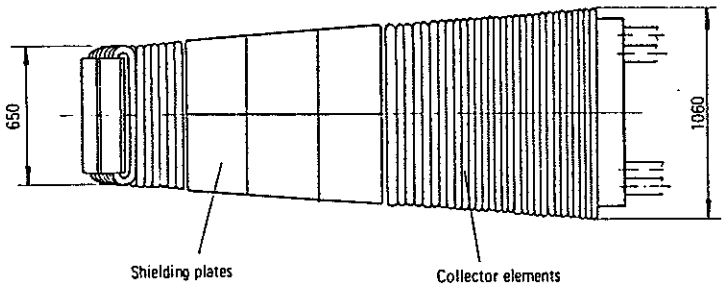

FIG. VIII-25. Example of divertor plate element.

7.6. Conclusions

An evaluation of the sputtering data gives a lifetime of about 2 years for the central part of the divertor plate. However, considerable uncertainties exist for the other potential lifetime-limiting mechanisms. Therefore, further experimental data are needed.

8. MECHANICAL DESIGN

The layout, structure and maintenance procedures of the divertor system are described in Section IV-5. The present section considers in particular the mechanical design of outer and inner collector plates, whose surfaces are subjected to erosion and sputtering from impinging ions. The plates are integrated within or applied to the structures of the 12 divertor modules.

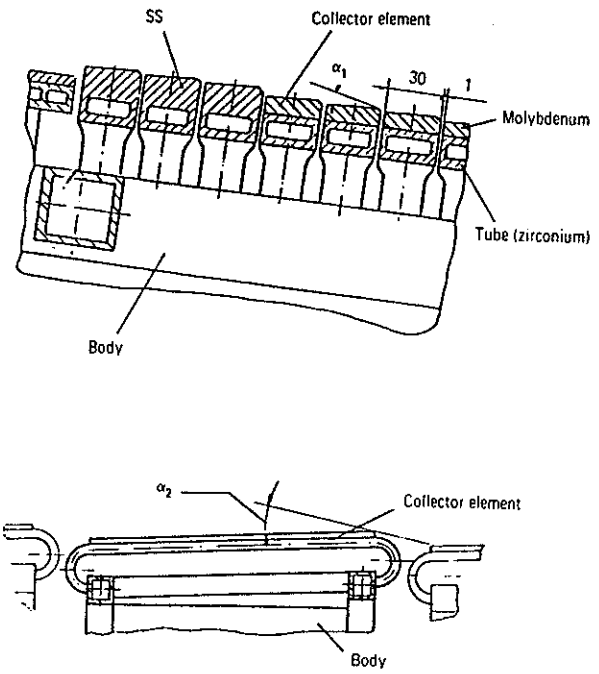

FIG. VIII-26. Cross-sections through the element of Fig. VIII-25.

Various design options are possible relative to the geometry, the coolant distribution, the number and arrangement of plate sub-assemblies, and the sequence of cooling of the various zones (for instance, series cooling or parallel cooling). This section describes only the primary design solutions of a plate sub-assembly or sub-module, which in general is made up of three components:

collector tiles
coolant channels or heat sinks
supporting structure, with the coolant header attachments.

8.1. Direction of the cooling channels

The cooling channels can be radially directed, following the profile of the plate, as indicated in Fig.VIII-24 (which shows a plate sub-module of the outer zone seen from below), or circumferentially directed, as illustrated by the examples in Figs VIII-25 and VIII-26. The first option requires that the pitch of the cooling

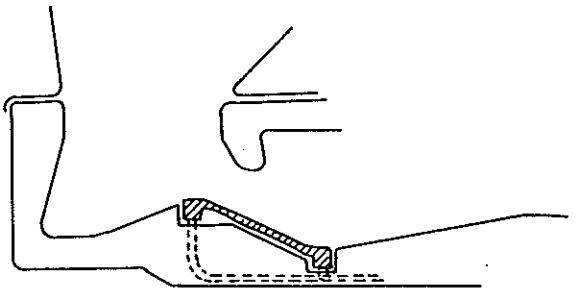

FIG. VIII-27. Scheme for the insertion of the divertor into the divertor chamber structure.

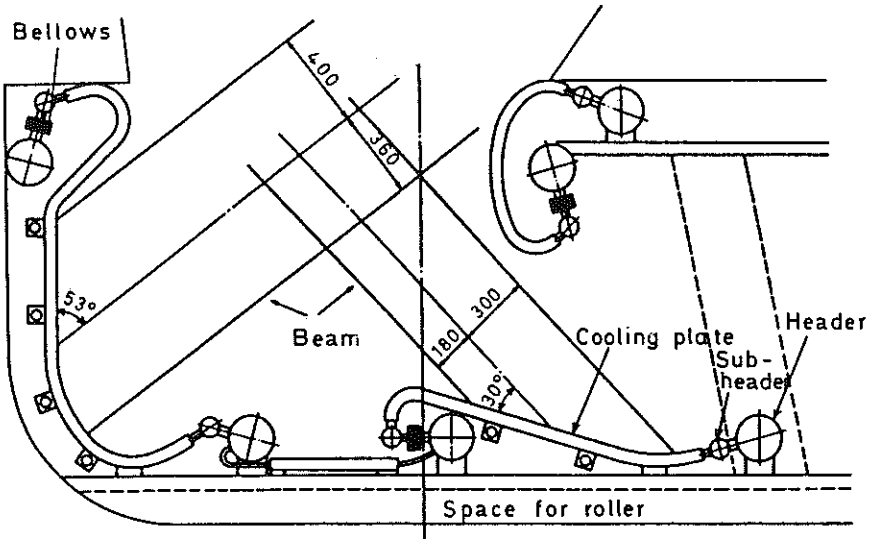

FIG. VIII-28. Example of the arrangement of the different elements of the divertor [3].

channels be varied in order to follow the increase of the surface with the major radius. This limits the concept to short sub-modules, in order to minimize the difference in pitch between inlet and outlet.

The second option has the disadvantage of requiring discontinuities between the adjacent sub-modules, in order to accommodate the inlet and outlet of the cooling channels (see Fig.VIII-26). This requires tilting of the plates, which increases the wall loading on all surfaces. In addition, gaps in the armour will

occur over the entire surface of the plate, from the inside to the outside, where high-energy neutrals can damage the cooling channels and the other structures below the tiles. Further analysis is needed to determine how severe this damage could be. Radial channels are the preferred option.

8.2. Integration of plate sub-modules and cooling headers

The plate sub-modules and the corresponding cooling headers can be integrated inside the profile of the body of the divertor module, as indicated in Fig.VIII-27, or can be separately applied on the supporting body, as indicated in Fig.VIII-28.

The first option ensures the most uniform protection by the tile and avoids exposing the headers and the other structural components to the erosion of the high-energy particles; therefore, it is the preferable option.

8.3. Joint between collector tiles and heat sink

The two main options discussed are the brazed concept, where the plates are part of a multi-layer structure with different layers brazed together (Fig.VIII-5), and the mechanically attached concept, where the collector tiles (mainly cooled by radiation) are mechanically connected to the underlying structure.

From a mechanical point of view, the principal advantage of the brazed concept is its simplicity of fabrication. The mechanically attached concept, on the other hand, requires precise fabrication and mounting in order to ensure the existence of the interspaces which are necessary to cope with the thermal expansion of the tiles at high temperatures. An advantage is that rows of tiles may be removed and replaced without disturbing the rest of the structure.

REFERENCES TO CHAPTER VIII

[1] INTOR GROUP, International Tokamak Reactor: Zero Phase (Rep. Int. Tokamak Reactor Workshop Vienna, 1979), International Atomic Energy Agency, Vienna (1980) 650 pp. *See also:* Summary in Nucl. Fusion 20 3 (1980) 349.

[2] Euratom Conceptual Design Contribution to the INTOR Phase-One Workshop, Rep. Commission of the European Communities, Brussels (1981).

[3] Japanese Conceptual Design Contribution to the INTOR Phase-One Workshop, Rep. Japan Atomic Energy Research Institute, Tokai-mura (1981).

[4] USA Conceptual Design Contribution to the INTOR Phase-One Workshop, Rep. INTOR/81-1, Georgia Institute of Technology, Atlanta, GA (1981).

[5] USSR Conceptual Design Contribution to the INTOR Phase-One Workshop, Rep. Kurchatov Institute, Moscow (1981).

[6] American Institute of Physics Handbook, McGraw Hill, New York (1957).
[7] Aerospace Structural Metals Handbook, Department of Defense, Washington, DC (1981).
[8] KNOLL, R.W., A Literature Review of Radiation Damage for Copper, Rep. UWFDM-384, Wisconsin Univ., Madison, Dept. of Nuclear Engineering (1980).
[9] MAKIN, M.J., Radiation Effects (Proc. Am. Metall. Soc. Conf.) Vol. 37 (1965) 627.
[10] ROTH, J., BOHDANSKI, J., OTTENBERGER, W., Data on Low Energy Light Ion Sputtering, Rep. IPP-9/26, Max-Planck-Institut für Plasmaphysik, Garching (1979).
[11] BATTY, J.C., STICKNEY, R.E., Oxid. Met. 3 (1971) 331.